Article

Glycopolypeptide Coordinated Nanovaccine: Fabrication, Characterization, and Antitumor Immune Response

Published as part of Chem & Bio Engineering virtual special issue "Engineering Nanomedicine".

Yingying Song, Lin Teng, Yanzheng Chen, and Chang-Ming Dong*

Cite This: Chem Bio Eng. 2024, 1, 633−646

Read Online

ACCESS | Metrics & More | Article Recommendations | Supporting Information

ABSTRACT: Cancer nanovaccine is a frontier immunotherapy strategy, in which the delivery carrier can protect antigen and adjuvant from degradation, increase blood circulation half-life, and improve antigen permeability and presentation, thus enhancing the security and potency of nanovaccine. To address the barriers of antigen delivery, we design and fabricate a kind of intracellular pH-sensitive glycopolypeptide coordinated nanovaccine (OVA-HPGM-Mn) with ∼30% loading capacity of ovalbumin (OVA). The nanovaccine OVA-HPGM-Mn could specifically deliver antigen to dendritic cells (DCs) and effectively escape from endolysosomes to cytoplasm after 6 h of incubation, while the blank counterpart HPGM-Mn acted as an adjuvant to promote DCs maturation and increase the percentage of matured cells to 26.5% from 11.8% in vitro. Furthermore, the mannosylated polypeptide nanovaccine prolonged the retention time of OVA for 72 h to facilitate 29.5% DCs maturation in lymph nodes, activated 48.8% CD8$^+$T cells in spleen, increased the CD8$^+$/CD4$^+$T cell ratio twice to 1.06, and upregulated the levels of pro-inflammatory cytokines including TNF-α, IFN-γ, and IL-6, thus inhibiting the tumor growth of ∼80%. Consequently, this work provides a versatile strategy for the fabrication of glycosylated polypeptide coordinated nanomaterials for antigen delivery and cancer immunotherapy.

KEYWORDS: glycopolypeptide nanoparticle, self-adjuvant, antigen delivery, glycopolypeptide nanovaccine, synergistic immunity, cancer immunotherapy
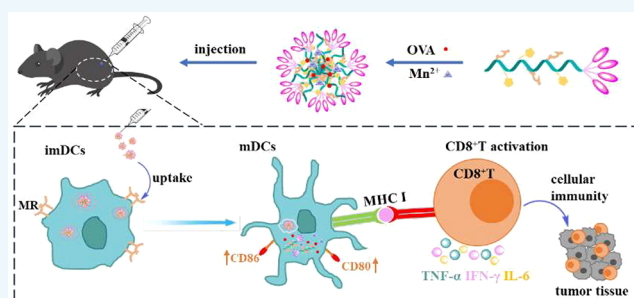
■ INTRODUCTION

Cancer immunotherapy, a strategy that triggers the host immune system to recognize and kill cancer cells, shows high specificity and potency and has made great progress in recent decades.[1−3] Cancer immunotherapies include immune checkpoint blockade immunotherapy,[4] cancer vaccines,[5] cell therapy,[6] therapeutic antibodies,[7] etc. Among them, cancer nanovaccines with high specificity and relatively low cost have attracted tremendous interests.[8−10] However, easy degradation, short blood circulation half-life, and poor membrane permeability of antigens often make the therapeutic effect limited. To improve therapeutic activity, the development of functional antigen delivery systems would be important. In recent years, great progress has been made in the design of nanocarriers for antigen delivery; nanocarriers have the advantages of protection, long-term circulation, controlled release, targeted drug delivery, etc., effectively improving the safety and effectiveness of antigens.[11−13] Among various delivery systems, pH-sensitive antigen nanocarriers (acidic endolysosomes, pH 4.5−6.5) can endogenously trigger antigen release and promote cross-presentation, thus enhancing cellular immunity. Therefore, various pH-sensitive antigen

vehicles have been constructed by physically encapsulation in hydrophilic cavities,[14−16] adsorbtion by electrostatic interactions,[17−19] physically embedded in the cross-linked micro/nano-gels,[20,21] loaded in the pH-sensitive metal coordination assemblies,[22−24] etc.

Metal ions are key components of various proteins in organisms and play an important role in the process of their biological activities.[25,26] In recent years, the role of metal ions in the immune response and tumor therapy has aroused great interest; among metal ions, manganese is one of the most studied elements. It is believed that manganese ions can increase the sensitivity of cyclic guanosine monophosphate-adenosine monophosphate synthase (cGAS) to double-stranded DNA and promote stimulator of interferon gene (STING) activation, i.e., as an agonist of the cGAS-STING
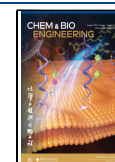
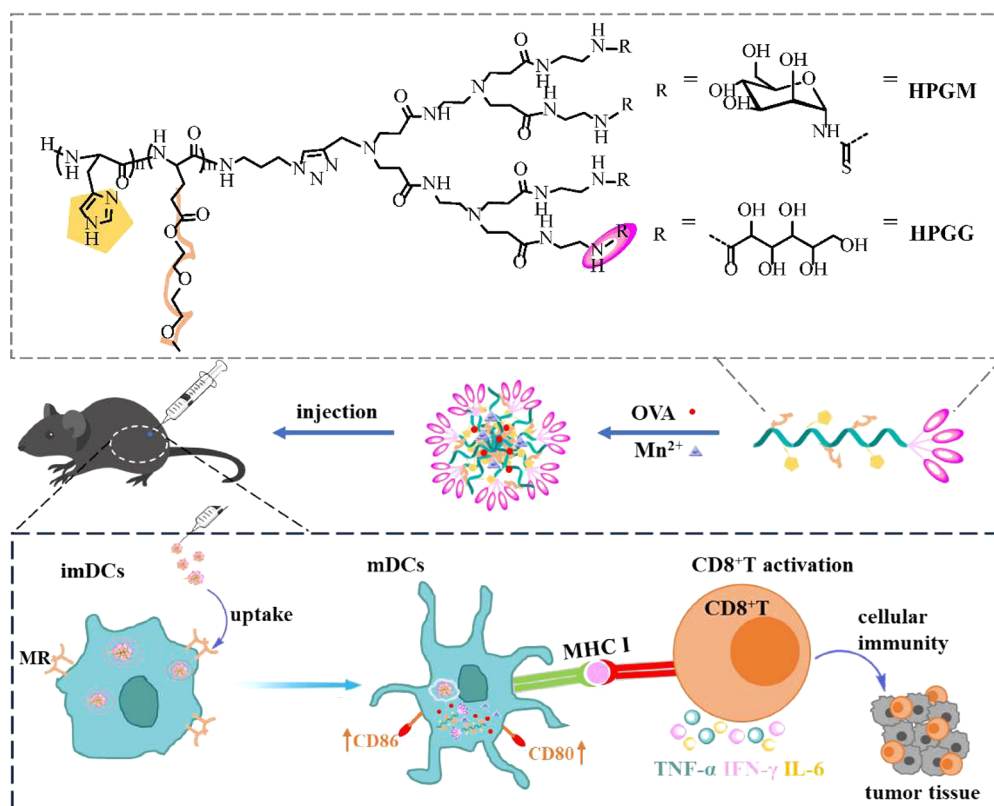Scheme 1. Preparation and Anti-Tumor Immune Response of the Glycopolypeptide Coordinated Nanovaccine

pathway. For example, Jiang et al. discovered manganese ions played dual functions of alarmin and agonist in the cGAS-STING pathway, promoting the secretion of type I interferon, then recruiting professional immune cells such as macrophages, dendritic cells, and lymphocytes and promoting the maturation and antigen presentation of dendritic cells, thereby activating immunity.[27−29] Through the coordination of manganese ions and imidazole groups, scientists have developed a variety of pH-sensitive coordination nanomaterials, which have promising applications in protein delivery and immunotherapy.[30,31]

Synthetic polypeptide is one of the candidate materials for drug delivery because of its desirable biocompatibility, biodegradability, and unique secondary conformations, and some polypeptide nanomedicines and hydrogels have entered clinical trials.[32,33] In the antigen delivery and immunotherapy fields, our group previously prepared photoresponsive vesicles by glycosylated polypeptide amphiphiles for antigen delivery, and the glucose-coated polypeptide vesicles effectively delivered antigen into cells and triggered release through UV-irradiation-induced morphology transformation, thus activating a cellular immune response.[34] Chen's group complexed polypeptide poly(L-phenylalanine)-b-poly(L-lysine) (PL-Phe-b-PL-Lys, PL-K) or poly(L-phenylalanine)-b-poly(D-lysine) (PL-Phe-b-PD-Lys, PD-K) with ovalbumin (OVA) via electrostatic interaction to develop chiral polypeptide nano-vaccines and found PD-K-OVA strongly promoted the maturation of DCs and the secretion of type-1 T helper cell cytokines more than PL-K-OVA, elicited robust antigen cross-presentation and adaptive immune response, and demonstrated better anticancer efficacy.[35] However, developing multifunctional polypeptide nanovaccines that can specifically deliver and release antigen into dendritic cells (DCs) and achieve potent efficacy is still challenging.

Exogenous antigens' efficient uptake and endolysosomal escape into cytoplasm by antigen present cells (APCs) is the prerequisite to induce immune response. However, most antigen delivery carriers lack targeting APCs, promoting fast antigen escape from the endolysosome, biodegradability and biosafety, and especially self-adjuvant activity like an agonist to enhance immunity. The imidazole-functionalized nanocarriers can significantly improve endolysosomes escape via proton sponge effect,[36,37] while the mannose moieties can specifically bind to the mannose receptor (MR) on antigen-presenting cells (APCs) to achieve APC targeting.[38,39] In this study, a kind of glycosylated polypeptide (PHGM/PHGG) composed of poly(Nτ-(2,4-dinitrobenzene)-L-histidine-co-diethylene glycol monomethyl ether glutamic acid) (PDHG) and dendritic mannose/glucose-periphery polyamidoamine (D2-Man/D2-Glu) was conjugated by click chemistry (Scheme S1), and the glycopolypeptide coordinated nanovaccine (OVA-HPGM-Mn) was simply constructed by multiple coordination interactions of pendant histidines, OVA, and manganese ions (Scheme 1). The as-designed nanovaccine could specifically bind to APCs and significantly improve the antigen uptake of the OVA; meanwhile, the proton sponge effect of imidazole groups remarkably promoted the antigen escape from the endolysosomes and enhanced the antigen presentation. Note that the blank glycopolypeptide nanoparticles (HPGM-Mn) themselves played the role of a kind of self-adjuvant to promote cell maturation. With subcutaneous injection of OVA-HPGM-Mn, the antigen retention time at injection site of mice was significantly prolonged even for 72 h. These characteristics made the mannose-tethered nanovaccine activate CD4^{+}/8^{+}T cells immune response and inhibit the tumor growth better than the glucose-tethered one.

■ EXPERIMENTAL SECTION

Materials. Copper(I) bromide (CuBr), N,N,N′,N″,N″-pentamethyldiethylenetriamine (PMDETA), fluorescein isothiocyanate (FITC), ovalbumin (OVA), and 3-(4,5-dimethylthiazol-2-yl)-2,5-diphenyltetrazolium bromide (MTT) were purchased from Sigma-Aldrich. Cy5 NHS-ester and N-(tert-butoxycarbonyl)-1-(2,4-dinitrophenyl)-L-histidine (Boc-L-His(DNP)−OH) were purchased commercially from Shanghai Yuanye Bio-Technology Co., Ltd. The second-generation alkynyl focal point poly(amido amine) dendron (D2), diethylene glycol-derived L-glutamate-N-carboxyanhydride (EG$_2$-Glu NCA), and 3-azido-1-propylamine were, respectively, synthesized according to our previous publications.[40,41] RPMI-1640, fetal bovine serum (FBS, GIBCO), Hoechst 33342, and LysoTracker Red were purchased from Beyotime Biotechnology (Shanghai, China). Recombinant mouse GM-CSF and IL-4 were purchased from Pepro Tech; anti-mouse ELISA kits (IL-6, IFN-γ, and TNF-α) were purchased from Shanghai Enzyme-linked Biotechnology (China). Fluorochrome-labeled anti-mouse monoclonal antibodies (CD11c-APC, CD80-FITC, CD86-PE) were purchased from Biolegend.

Methods. ^{1}H NMR (400 MHz) spectroscopy was recorded on a Varian Mercury-400 spectrometer at room temperature. CDCl$_3$, DMSO-d_6, and D$_2$O were used as solvents for various NMR measurements. Fourier transform infrared (FT-IR) spectroscopy was recorded on a Perkin Elmer Spectrum 100 spectrometer at frequencies ranging from 400 to 4000 cm^{-1} at room temperature, and the solid sample was mixed with KBr and pressed into a pellet form before measurement. Molecular weights and polydispersities (M_w/M_n) of polymers were measured by gel permeation chromatography (GPC) equipped with two HLC-8320 columns (TSKgel Super AWM-H, pore size: 9 μm; 6 × 150 mm, Tosoh, Japan) and a double-path, double-flow refractive index (RI) detector (Bryce) at 30 °C. The elution phase was running with DMF-LiBr (0.01 mol/L) at 0.6 mL/min, and the calibration curve was obtained by standard poly(methyl methacrylate). UV–Vis spectra were recorded at room temperature by using a Spectrumlab54 spectrophotometer. The hydrodynamic diameter (D_h) and polydispersities of nanoparticles were determined by dynamic light scattering (DLS) using a Malvern Nano S instrument (Malvern, UK) that was performed at a scattering angle of 90° and 25 °C. All the measurements were repeated five times, and the average values reported were the mean diameter ± standard deviation. Transmission electron microscopy (TEM) was performed without negative staining by using a JEM-2100 at 200 kV accelerating voltage, in which the nanoparticles solution was dropped onto the surface of 230 mesh carbon-coated copper grids and lyophilized before measurement. X-ray photoelectron spectroscopy (XPS) was conducted on a Kratos Axis Ultra DLD photoelectron spectroscope (AXIS UltraDLD, Japan). Cellular uptake was recorded by flow cytometry (BD, LSR Fortessa, UK). Fluorescence images were obtained on a confocal laser scanning microscope (CLSM) imaging system (Leica, TCS SP8 STED 3X, Germany).

Synthesis of Azido-Terminated Copolypeptide. Diethylene glycol-derived L-glutamate-N-carboxyanhydride (EG$_2$-Glu NCA) and N$_τ$-(2,4-dinitrophenyl)-L-histine-N-carboxyanhydride (DNP-His NCA) were firstly synthesized according to previous publications,[40,41] but some changes were made for preparation of DNP-His NCA and were described in detail in Supporting Information. Then azido-terminated poly(N$_τ$-(2,4-dinitrophenyl)-L-histine)-r-poly(diethylene glycol-L-glutamate) (PDHG) was prepared by the ring-opening polymerization of DNP-His NCA and EG$_2$-Glu NCA in dry DMF using 3-azido-1-propylamine as an initiator. DNP-His NCA (221.0 mg, 0.637 mmol) and EG$_2$-Glu NCA (175.0 mg, 0.637 mmol) were dissolved in 8 mL of dried DMF in a glovebox, and then 3-azido-1-propylamine in DMF (47.0 μL, 0.159 mmol) was added. The resulting solution was stirred for 24 h at room temperature and then precipitated dropwise into a large excess of diethyl ether (50 mL). The light yellow precipitate was centrifuged and dried in vacuo to give 265.0 mg of PDHG (77.9 %, yield). ^{1}H NMR of PDHG (DMSO-d_6): δ (ppm) = 8.90 (br, N-CCH═CHC(NO$_2$)═CHC(NO$_2$), 4H), 8.65

(br, NCCH═CHC(NO$_2$)═CHC(NO$_2$), 4H), 8.02−7.82 (m, CHCH$_2$C(═CH) N═CH & N−CCH═CHC(NO$_2$)═CHC(NO$_2$), 8H), 7.23 (br, CHCH$_2$C═CH, 4H), 4.52 (br, CHCH$_2$C═CH, 4H), 4.23 (br, CHCH$_2$CH$_2$CO, 4H), 4.14−4.04 (m, CH$_3$OCH$_2$CH$_2$OCH$_2$CH$_2$, 8H), 3.66−3.26 (m, N$_3$CH$_2$CH$_2$CH$_2$ & CH$_3$OCH$_2$CH$_2$OCH$_2$CH$_2$, 26H), 3.19 (s, CH$_3$OCH$_2$CH$_2$, 12H), 3.11 (br, N$_3$CH$_2$CH$_2$CH$_2$,2H), 3.06−2.72 (m, CHCH$_2$C═CH, 8H), 2.43−2.16 (m, CHCH$_2$CH$_2$CO, 8H), 2.04−1.66 (m, CHCH$_2$CH$_2$CO, 8H), 1.62 (br, N$_3$CH$_2$CH$_2$CH$_2$, 2H). FT-IR (KBr, cm^{-1}): 3300 (νN−H), 2099 (νN$_3$), 1734 (νC−O), 1654 (amide I), 1525 (νNO$_2$), 1131 (νC−O−C).

Preparation of Glycosylated Polypeptide Copolymers. Mannose or glucose decorated D2 (D2-Man or D2-Glu) was connected with PDHG via copper(I)-catalyzed azide−alkyne cycloaddition (CuAAC).[42] In a representative example, the CuAAC reaction between alkyne focal point D2-Man (52.0 mg, 0.033 mmol) and azide-terminated PDHG (60.0 mg, 0.027 mmol) was conducted at 35 °C in 6 mL of DMSO with CuBr (3.8 mg, 0.027 mmol) and PMDETA (6.5 μL, 0.027 mmol) as catalysts. After 24 h, EDTA aqueous solution (1.5 mL, 30 mg/mL) was added to the resulting solution to combine copper ions, and then the solution was transferred to a dialysis bag with 1000 Da molecular cutoff and dialyzed against water for 2 days. The resulting solution was put under reduced pressure to remove water, and the sample was redissolved in 8 mL of DMSO. Then mercaptoethanol (200 μL, 2.841 mmol) was added and stirred for 24 h at room temperature under N$_2$ atmosphere. The solution was diluted with an equal volume of dichloromethane and precipitated in diethyl ether, and the light yellow solid was centrifugated, washed five times with diethyl ether, and dried in vacuo to give 57.0 mg of mannose-decorated polypeptide (PHGM, 73.0%, yield). 65.0 mg of glucose-decorated polypeptide (PHGG, 76.0%, yield) was obtained with the same method.

Construction of Glycopolypeptide Coordinated Nanoparticles. Nanoparticles made of OVA and PHGM/PHGG were assembled in 50 mM pH 8.0 HEPES media by addition of MnCl$_2$ solution. 4 mg of PHGM/PHGG was dissolved in 2 mL of HEPES and mixed with the solution of 2 mg of OVA in 2 mL of HEPES at 4 °C. After 2 h stirring, an appropriate volume of an aqueous solution of MnCl$_2$ was added, and stirring was continued overnight; the solution changed milky, and nanoparticles formed. The nanoparticles were collected by centrifugation at 12,000 rpm for 10 min and washed twice with HEPES, redispersed, and stored at 4 °C for further use.

pH-Responsive Release of OVA from Coordinated Nanoparticles. The standard curve of Cy5-OVA was obtained by testing the UV-absorption from 400 to 800 nm of a series of Cy5-OVA solutions with fixed concentration, and the concentrations of Cy5-OVA were plotted against absorption intensity at 646 nm.

The pH-responsive release experiment was conducted by a dialysis method as described in previous publications. 2.0 mL of Cy5-OVA coordinated nanoparticles solution was placed in a dialysis bag (MWCO 100k Da) and immersed in 8 mL of PBS in a tube at different pH values (7.4 and 5.0), at 37 °C with constant shaking at a rate of 150 rpm. 2 mL of dialysis medium was removed periodically; meanwhile, into that medium was placed another 2 mL of fresh PBS. The UV-Vis spectra were recorded, and the released amounts of Cy5-OVA were calculated from the standard curve ($n = 3$).

Bone Marrow-Derived Cells (BMDCs) Extraction. BMDCs were isolated from the bone marrow of C57BL/6 mice (female, 6−8 weeks old).[43,44] Femurs and tibias were removed from the mice, eliminating muscles and tissue, ensuring the epiphysis remained intact. After washing with RPMI-1640, both ends of the bones were trimmed using sterile scissors to expose the interior marrow shaft; then, the contents of marrow were flushed out with RPMI-1640 using a syringe needle. After they passed through a 70 μm cell sieve and were centrifugated, the cells were seeded on 100 mm petri dishes at a density of 1 × 10^7 cells mL^{-1}, and BMDCs were induced in RPMI-1640 containing 20 ng/mL GM-CSF, 5 ng/mL IL-4, and 2 mM L-glutamine. The culture medium was changed every 2 days, and immature BMDCs can be acquired in 7 days.
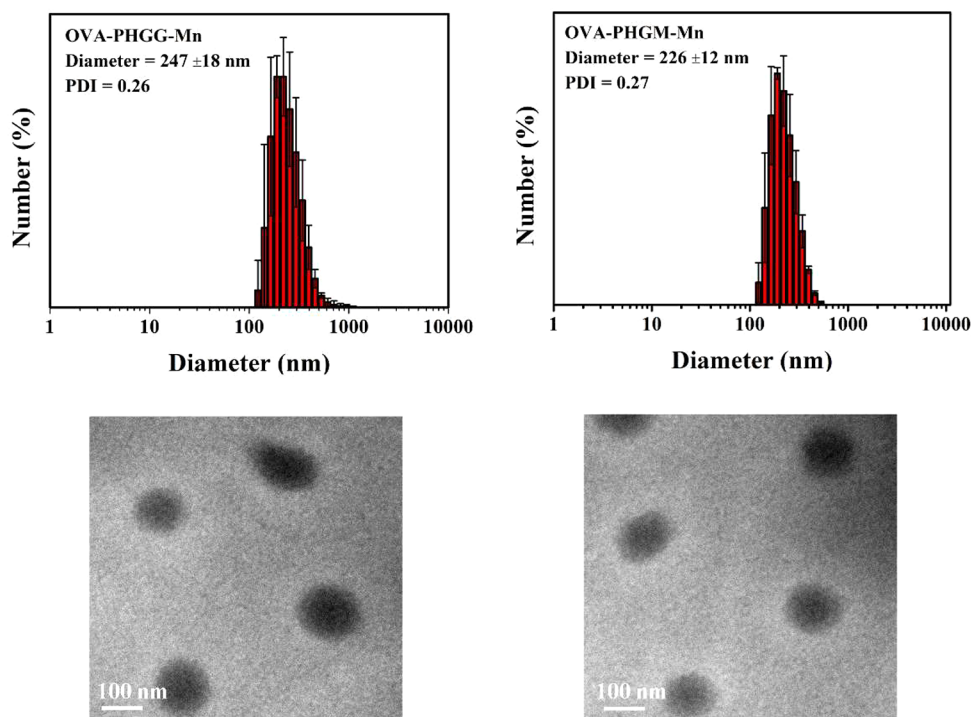
Figure 1. DLS and TEM photographs of the self-assembled nanoparticles of the OVA-PHGG-Mn and the OVA-PHGM-Mn.

In Vitro Biocompatibility. The hemolytic performance of the prepared coordinated nanoparticles was evaluated as previously reported.[45] 100 μL of various concentrations (400, 200, 100 μg/mL) of nanoparticles was soaked in 500 μL of Sprague Dawley (SD) rat blood containing sodium citrate anticoagulant and incubated at 37 °C for 3 h. The blood was centrifuged at 1000 rpm for 10 min, and then 100 μL of supernatant was taken out and diluted to 3 mL with deionized water. UV absorption at 540 nm was recorded, and then the hemolysis ratio was calculated according to the formula: hemolysis ratio (%) = (OD$_{sample}$ − OD$_{PBS}$) / (OD$_{Triton-X}$ − OD$_{PBS}$) × 100%, where OD represents the absorption value at 540 nm. All experiments were repeated three times ($n = 3$), and PBS and 1% Triton X-100 were, respectively, used as negative and positive controls.

Cell viability was performed according to a standard MTT assay. BMDCs were seeded on 96-well plates at a density of 1×10^4 cells per well and cultured overnight. After the culture media were removed, fresh culture media containing different concentrations of coordinated nanoparticles (12.5, 25, 50, 100, and 200 μg/mL) were added and further cocultured for 48 h. Subsequently, MTT solution in PBS (5 mg/mL) was added and incubated for another 4 h; then DMSO was added to dissolve the formazan, and the absorption values at 490 nm were recorded by a Microplate Reader. Cell viability = (OD$_{sample}$ − OD$_{blank}$) / (OD$_{control}$ − OD$_{blank}$), where OD$_{control}$ and OD$_{sample}$ were obtained in the presence of nanoparticles, respectively, and all experiments were repeated for six times ($n = 6$).

Cellular Uptake and Intracellular Localization. BMDCs were seeded on 6-well plates at a density of 5×10^5 cells per well and incubated overnight. Then FITC-OVA coordinated nanoparticles (10 μg/mL equiv) or free FITC-OVA were added and cocultured with BMDCs for 4 h at 37 °C. In an experiment of evaluation of sugar-targeting effect on cellular uptake, 100 mM mannose was added 1 h prior to addition of nanoparticles. After 4 h, the cells were washed and collected, and then the fluorescence intensity was analyzed by flow cytometer to measure internalized FITC-OVA.

For the test of intracellular localization, DC2.4 cells were incubated with FITC-OVA coordinated nanoparticles (10 μg/mL equiv) for 6 and 10 h, then washed with PBS twice. The nuclei and lysosomes were stained with Hoechst 33342 and LysoTracker red (50 nM), respectively. After washing with PBS and fixing with 4% paraformaldehyde, the cells were observed with CLSM.

In Vitro BMDCs Activation and Cytokine Secretion. For in vitro BMDCs maturation experiments, immature BMDCs were seeded into 24-well plates at a density of 5×10^5 mL^{-1} and cocultured with free OVA, blank coordinated nanoparticles, and OVA containing coordinated nanoparticles for 24 h. Subsequently, cells were harvested and stained with anti-CD11c APC, anti-CD86 PE, and anti-CD80 FITC for 30 min, then analyzed by flow cytometry. The culture supernatant was collected to analyze the levels of TNF-α, IL-6, and IFN-γ using enzyme-linked immunosorbent assay (ELISA) kits ($n = 3$).

Retention of Antigen at Injection Site. BALB/c mice were subcutaneously injected at the posterior end with Cy5-OVA or Cy5-OVA coordinated nanoparticles (50 μg of OVA in 100 μL of HEPES per mouse). The presence of OVA in the injection site was recorded at four time points (6, 24, 48, and 72 h) post injection by fluorescence images. The fluorescence intensity at different times was analyzed by Living Images Software.

In Vivo Antitumor Assay. To evaluate the antitumor efficacy of the OVA coordinated nanoparticles, C57BL/6 mice (female, 6 weeks) were subcutaneously inoculated with B16-OVA melanoma cells (1×10^7 cells) into the right flank of each mouse to obtain the melanoma-bearing model. Mice were randomly divided into six groups when the tumor volumes reached 70−80 mm^3, and then different samples (HEPES, OVA, blank nanoparticles, coordinated nanovaccines, and OVA equiv = 50 μg/per mouse) were subcutaneously injected near the tumor on days 6, 10, and 14. The tumor size and body weight of each mouse were recorded every other day. The tumor size was calculated according to the following formula: width^2 × length × 0.5. The mice were all sacrificed on day 19; the tumors were isolated and weighed to calculate tumor inhibition ratio. Both isolated major organs (heart, liver, spleen, lung, and kidney) were fixed in 4% paraformaldehyde and dyed by hematoxylin with eosin (H&E) for histopathological evaluation. Tumors were extracted for H&E, TUNEL, and immunofluorescence analysis.

Single-cell suspension of splenocytes was stained with anti-CD3 APC, anti-CD4 PE, anti-CD8a FITC, and anti-CD45 Alexa Fluor 700 to analyze the percentage of OVA-specific CD8+T cells by flow cytometry. The lymph nodes were isolated from mice and treated to obtain single-cell suspension and then stained with anti-CD11c APC, anti-CD86 PE, and anti-CD80 FITC and analyzed by flow cytometry

to evaluate the maturation of DCs in vivo. Blood was collected from eyeballs, and the levels of IFN-γ, IL-6, and TNF-α in serum were measured by ELISA kits.

RESULTS AND DISCUSSION

Fabrication of OVA-Loaded Glycopolypeptide Coordinated Nanovaccine. To achieve a glycosylated polypep-

Table 1. Diameter of the Coordinated Nanoparticles before and after Loading of the OVA

Entry	D_h (nm)[a]	PDI[a]	Diameter (nm)[b]	LC (%)
HPGG-Mn	199 ± 11	0.12	120 ± 10	
OVA-HPGG-Mn	247 ± 18	0.26	137 ± 12	29.3
HPGM-Mn	182 ± 16	0.26	118 ± 8	
OVA-HPGM-Mn	226 ± 12	0.27	127 ± 10	30.1

[a]Hydrodynamic diameter (D_h) and polydispersities determined by DLS. [b]Average diameter was averaged by about 20 nanoparticles as determined by TEM; LC: loading capacity.

tide with suitable coordination capacity, a histidine unit that can coordinate with various metals was introduced into the polypeptide block. So, diethylene glycol-derived L-glutamate NCA (EG$_2$-Glu NCA) was copolymerized with DNP-His NCA to produce an azide-terminated polypeptide, click conjugated with alkynyl-focal point D2-Man and D2-Glu,

and then followed by removing protective groups of DNP to acquire the glycosylated polypeptides of mannose-tethered PHGM and glucose-tethered PHGG (Scheme S1), and ^{1}H NMR, FT-IR, and GPC were measured to confirm molecular structures. The characteristic signals of mannose or glucose residues in PHGM or PHGG were observed at 3.3−3.7 ppm while those of pendant histidines appeared at 7.0 and 8.0 ppm (Figure S1). In FT-IR spectra (Figure S2a), the characteristic peak at 2100 cm^{-1} assignable to the azido group completely disappeared after conjugation while a broad peak of 3300 cm^{-1} attributed to hydroxyl groups of sugar appeared. Moreover, the GPC curves (Figure S2b) showed a single peak of the polypeptide precursor, but a shoulder peak existed after conjugation probably due to the interactions between hydroxyls and chromatographic column.[46]

Imidazole groups have the ability to coordinate with a variety of metals.[47−49] Herein, we utilized the coordination interactions between manganese ions and imidazoles of PHGM or PHGG to construct blank nanoparticles, which could further coload OVA to form the OVA-loaded nanovaccines by the interactions between manganese ions with free carboxyls and imidazoles of OVA. The loading capacity of OVA in coordinated assemblies was around 35%, so we fixed PHGM and OVA at 1 and 0.5 mg/mL, respectively, then adjusted the molar ratio of manganese ions to histidine unit and investigated its effect to size of nanoparticles. As listed in
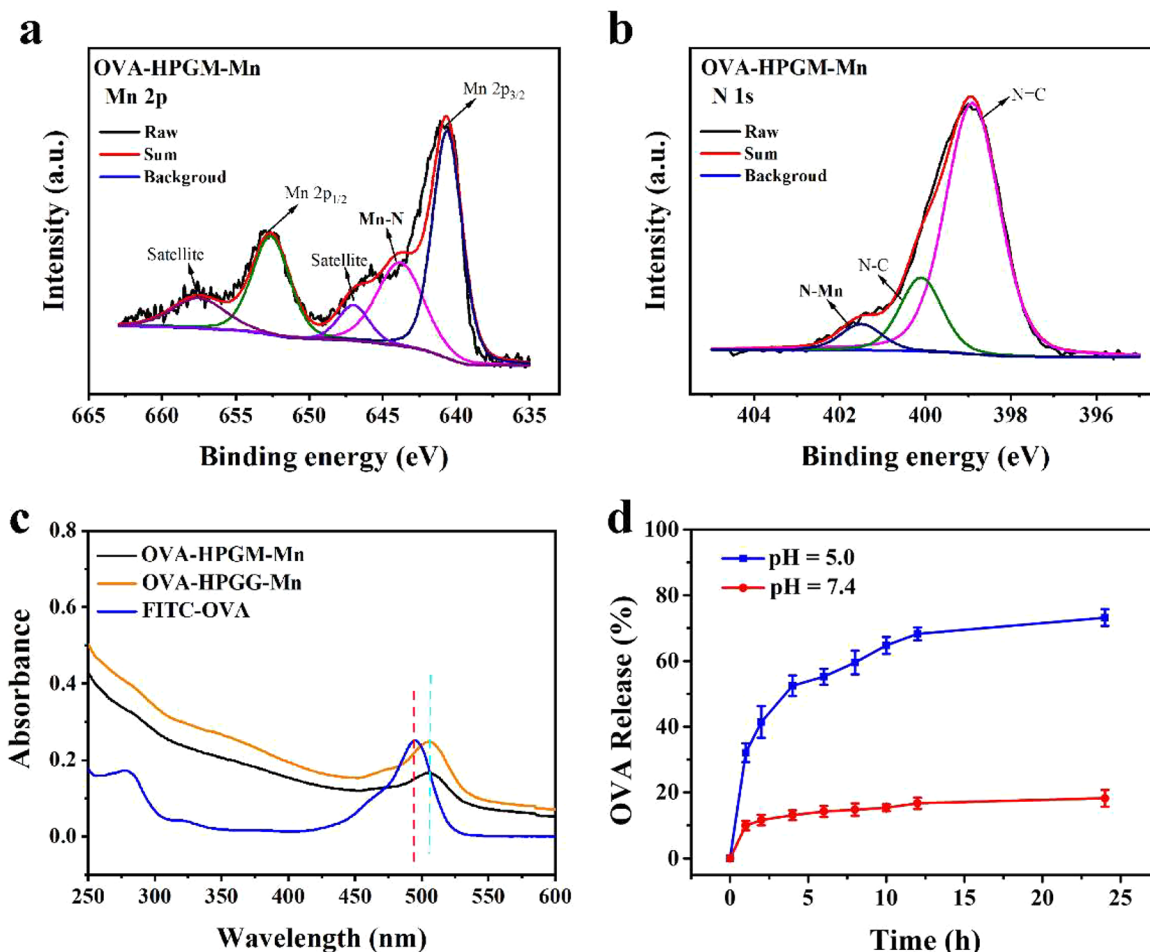

Figure 2. XPS spectra for (a) Mn 2p and (b) N 1s of OVA-HPGM-Mn; (c) UV-Vis spectra of free FITC-OVA and the coordinated nanoparticles containing FITC-OVA; (d) OVA release profiles of nanoparticles Cy5-OVA-PHGM-Mn at pH 5.0 and 7.4.
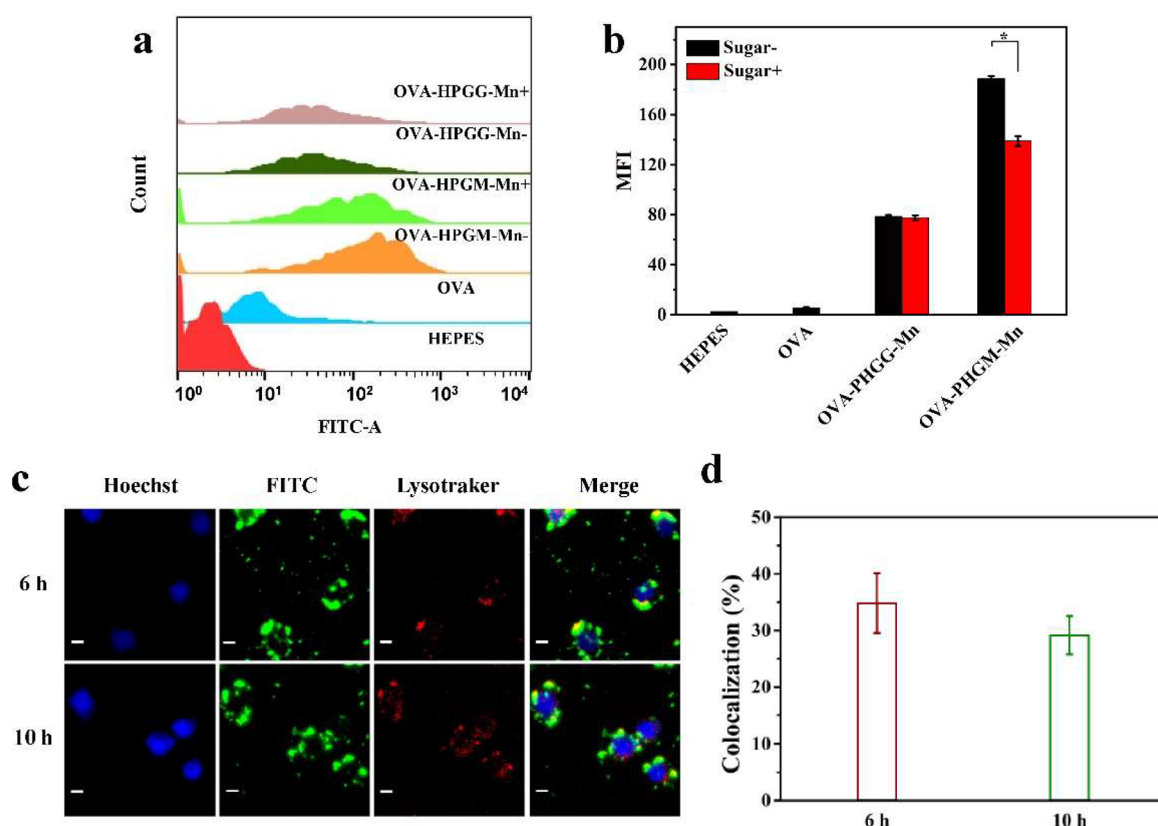
Figure 3. (a) Flow cytometry curves and (b) histograms of FITC-OVA loaded nanoparticles with DC cells for 4 h and the monosaccharide inhibition experiment ($n = 3$, $p^* < 0.05$); (c) CLSM images of DC 2.4 cells incubated with OVA-PHGM-Mn for 6 and 10 h (FITC-OVA = 10 μg/ mL, scale bar = 10 μm); (d) Colocalization of FITC-OVA-PHGM-Mn and LysoTracker-labeled endolysosomes at different incubation times calculated by ImageJ ($n = 10$).

Table S1, the OVA-loaded nanoparticles gave an average size of 226 ± 12 nm when the molar ratio of manganese ions to histidine was 3:1 while larger particles would form whether the content of manganese ions was higher or lower than 3:1. Therefore, we established the fabrication conditions (pH 8.0, $C_{polymer}/C_{OVA}$ = 1:0.5 (mg/mL), $[Mn^{2+}]$/histidine = 3) to construct the blank nanoparticles and OVA-loaded counterparts for subsequent study. The size and morphology of nanoparticles were evidenced by DLS and TEM, and the detailed results were shown in Figure 1, Figure S3, and Table 1. HPGM or HPGG formed spherical micellar aggregates around 200 nm; however, they increased to 220−250 nm with lower contrast compared to blank ones as the latter had relatively less Mn^{2+} content. Both OVA-HPGG-Mn and OVA-HPGM-Mn had good OVA-loading capacity of 30.1% and 29.3%, respectively, as calculated by UV-Vis spectroscopy. OVA-HPGG-Mn and OVA-HPGM-Mn had almost identical characters due to the same structure besides having mannose and glucose binding moieties, so subsequent measurements were taken using OVA-HPGM-Mn as an example.

To determinate coordinative interactions between manganese ions and histidines, the XPS spectra of OVA-HPGM-Mn were measured in Figure 2a,b, which showed the peaks of 643.8 eV in Mn 2p and 401.5 eV in N 1s, indicating the presence of Mn−N interactions,[50,51] and the content of manganese ions in OVA-PHGM-Mn was 5.1% as calculated by XPS. As XPS was generally used for surface elemental analysis, its value might be lower than the actual one. So ICP-MS was conducted to further determine the content of manganese ions,

which was 7.1% and relatively higher than that with XPS. UV-Vis spectra shown in Figure 2c demonstrated the characteristic peak of FITC-OVA shifted to 505 nm in OVA-HPGM-Mn from 495 nm of free OVA, also suggesting OVA was coordinated to forming the nanovaccine.

Imidazoles would be protonated under acidic pH that disrupted the metal-coordination bonds, endowing the nanoparticles with pH-sensitivity.[52,53] As expected, the OVA-HPGM-Mn would experience a weakly acidic microenvironment of endolysosomes after cell uptake. Therefore, the release behavior of OVA-HPGM-Mn was tested at pH 7.4 and 5.0, as shown in Figure 2d. It displayed a sustained release rate of 18.2% at pH 7.4 within 24 h; however, the release rate significantly increased to 52.0% at pH 5.0 in 4 h and reached 73.2% in 24 h. This is because the imidazoles in pendant histidines were protonated at pH 5.0, inducing disassembly of OVA-HPGM-Mn to facilitate the release of OVA. This acidic pH-sensitive disassembly was further supported by DLS and TEM, and the bigger nanovaccines nearly disrupted completely after being incubated at pH 5.0 (Figure S4).

Cellular Uptake and BMDCs Activation. In vitro hemocompatibility and cytotoxicity were first tested by a hemolytic test and MTT, respectively. As shown in Figure S5a, the hemolysis ratios of HPGM-Mn, HPGG-Mn, OVA-HPGM-Mn, and OVA-HPGG-Mn were all below 0.5% when the concentrations were less than 400 μg/mL, which were far less than the threshold value of 5% for biomaterials. Cytotoxicity of nanoparticles was assessed by a normal MTT assay using BMDCs as shown in Figure S5b. The cell viability was above
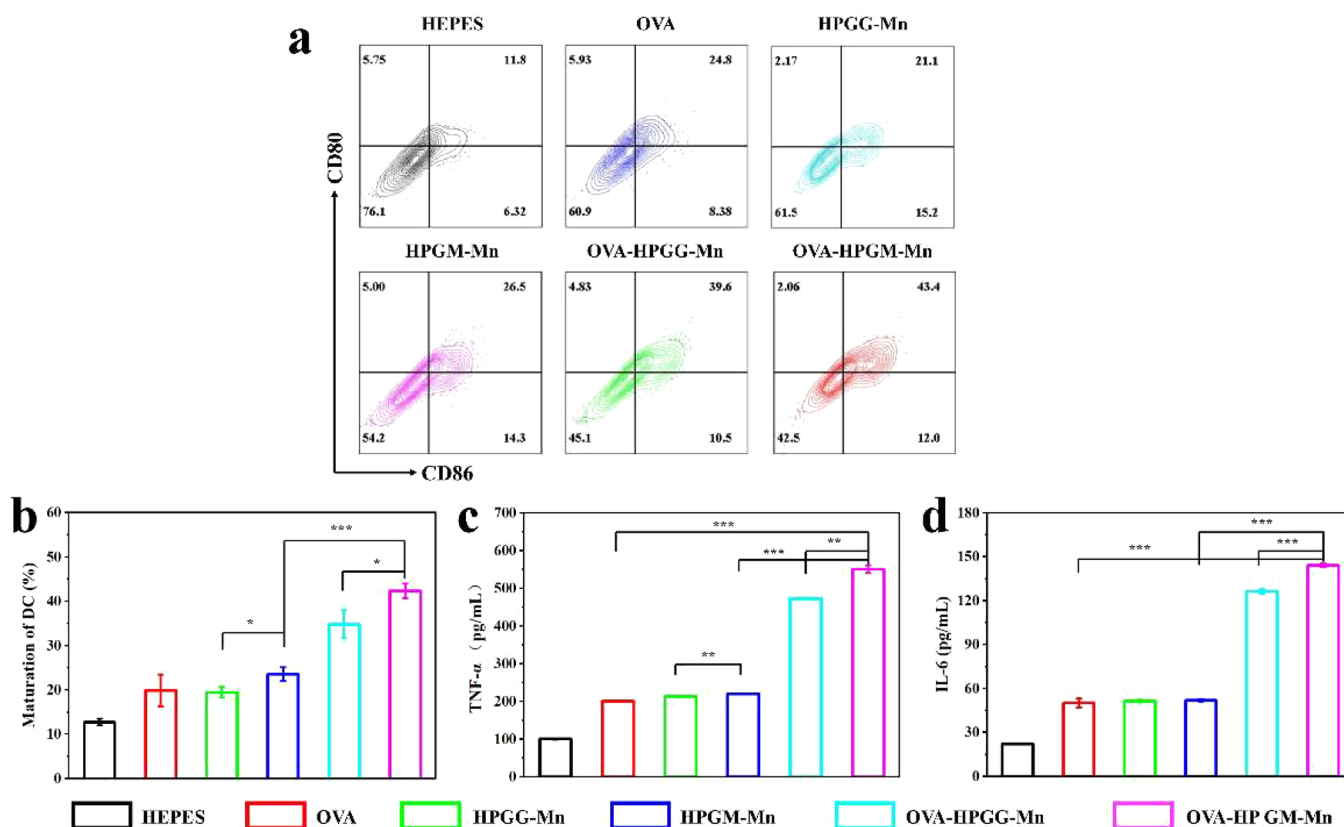
Figure 4. (a) Flow cytometry of BMDCs maturation induced by coordinated nanoparticles in vitro. (b) Histograms of BMDCs maturation induced by coordinated nanoparticles; the secreted concentrations of (c) TNF-α and (d) IL-6 when BMDCs treated with coordinated nanoparticles ($n = 3$, $p^* < 0.05$, $p^{**} < 0.01$, $P^{***} < 0.001$).

95% after co-incubation for 48 h with HPGM-Mn, HPGG-Mn, OVA-HPGM-Mn, or OVA-HPGG-Mn within 200 μg/mL, indicating less toxicity to BMDCs.

Dendritic cells are the most important antigen-presenting cells; whether they could effectively uptake, process, and present to T cells by APCs is prerequisite for adaptive cell immunity. Therefore, we used BMDCs to trace the cellular uptake process. As shown in Figure 3a,b, both OVA-PHGG-Mn and OVA-PHGM-Mn dramatically enhanced the uptake of OVA compared to free FITC-labeled OVA when co-cultured at 10 μg/mL within 4 h. Besides, the mean fluorescence intensity (MFI) of the internalized OVA-PHGM-Mn by BMDCs was 2.4-fold higher than that of the incubated OVA-PHGG-Mn after incubation for 4 h. Meanwhile, the MFI of OVA-PHGM-Mn internalized by BMDCs decreased about 26.5% when the cells were first treated with free mannose for 1 h but without remarkable change for OVA-PHGG-Mn, which could be explained by the specific binding between OVA-HPGM-Mn and mannose receptor (MR) expressed on BMDCs.[54,55] The same phenomenon was observed by a fluorescence microscope (Figure S6). Similarly, both OVA-PHGG-Mn and OVA-PHGM-Mn internalized by BMDCs showed higher fluorescence intensity compared to free FITC-OVA, indicating more efficient cellular uptake. Notably, effective subcellular escape of antigen from endolysosomes to cytoplasm is essential for processing, presentation, and induction of immune response. So, the co-localization of FITC-labelled OVA-HPGM-Mn and lyso tracker-labelled endolysosomes at different times was investigated by confocal laser-scanning microscopy (CLSM, Figure 3c,d). The colocal-

ization percentages of OVA-HPGM-Mn and endolysosomes were about 35% and 29% after 6 and 10 h of incubation, respectively, demonstrating most of the OVA antigen escaped into cytoplasm. The excellent subcellular escape ability of OVA-HPGM-Mn was due to the proton sponge effect of imidazole groups on the side chain of glycopolypeptide,[56,57] which is beneficial for enhancing adaptive cellular immunity. In addition, taking account of the endolysosome escape of antigen, the mannosylated poly(L-histidine) nanocarrier seems to surpass the related mannosylated or glucosylated poly(L-lysine) ones, which also needs detailed investigation to rationalize the glycopolypeptide nanocarrier for effective antigen delivery.[34,58,59]

Upon antigen uptake, immature DCs will digest antigens into peptides and present them to T cells and, meanwhile, convert into mature status by expressing costimulatory molecules. The capability of nanoparticles to stimulate BMDCs maturation was assessed by the expression levels of CD80 and CD86, as typical markers of mature DCs. The flow cytometry results in Figure 4a,b showed that the percentage of matured cells increased up to 21.1% and 26.5% from 11.8% when respectively treated with HPGG-Mn and HPGM-Mn, indicating an adjuvant effect of blank nanoparticles to promote DCs maturation. Both OVA-HPGG-Mn and OVA-HPGM-Mn triggered more significant DCs maturation than blank counterparts, and the mannose-tethered OVA-HPGM-Mn achieved the highest percentage of 43.4%, because specific binding of mannose-tethered nanovaccines with the MR of DCs would enhance OVA cellular uptake and antigen-presentation, thus boosting the maturation level. Furthermore,
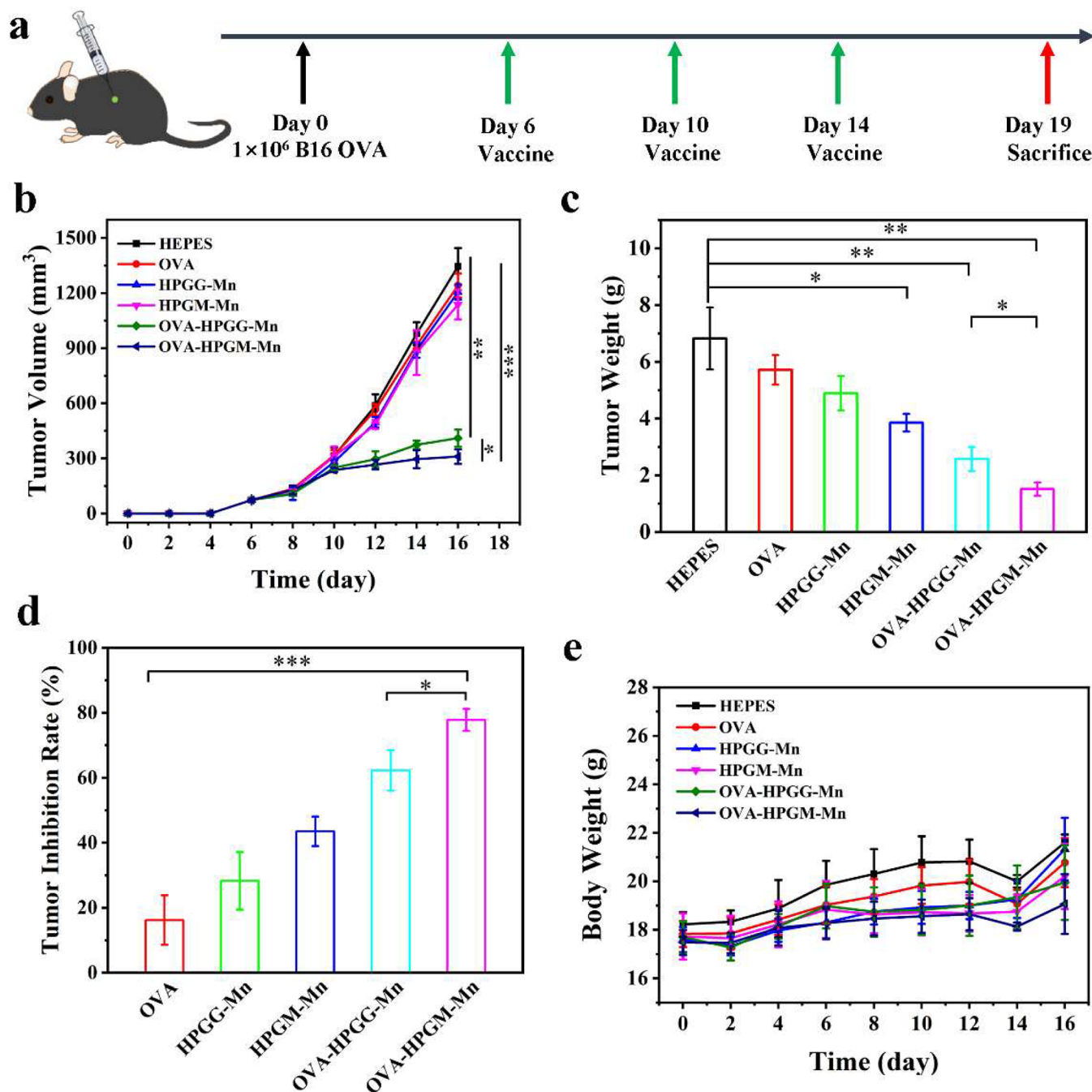
Figure 5. (a) Timeline (days) of tumor inoculation and vaccines injection; (b) tumor growth curves during treatments, (c) tumor weight, (d) tumor inhibition rate, and (e) body weight after various treatments ($n \geq 3$, $p^* < 0.05$, $p^{**} < 0.01$, $P^{***} < 0.001$).

we tested the secretion levels of TNF-α and IL-6 that are highly relevant to maturation by ELISA kits. As shown in Figure 4c,d, the concentration of TNF-α dramatically increased to ~200 pg/mL when incubated with HPGG-Mn and HPGM-Mn, indicating the adjuvant effect of blank glycopolypeptide nanoparticles. Remarkably, the level of TNF-α boosted to 500 and 580 pg/mL, further demonstrating the OVA-loaded nanovaccines played synergistic immunity-priming effect between self-adjuvant of blank nanoparticles and the loaded OVA antigen, and OVA-HPGM-Mn performed the best. Similarly, the level of IL-6 showed a similar tendency with TNF-α, all of which supported the fact that the OVA-loaded glycopolypeptide nanovaccines could effectively stimulate the

maturation of BMDCs to achieve effective antigen presentation. Taken together, these data demonstrate that blank nanoparticles of HPGG-Mn and HPGM-Mn presented immune self-adjuvant functions to promote BMDCs maturation, and their OVA-loaded nanovaccines of OVA-HPGG-Mn and OVA-HPGM-Mn could further activate BMDCs to secrete lots of immune-related cytokines, showcasing a synergistic immune-activating effect between the glycopolypeptide self-adjuvant with the loaded OVA antigen. Note that the comparison between our glycopolypeptide nano-adjuvant with commercial aluminum adjuvants, including aluminum hydroxide adjuvant and aluminum phosphate adjuvant, and synergistic immune mechanism of the glycopolypeptide nano-
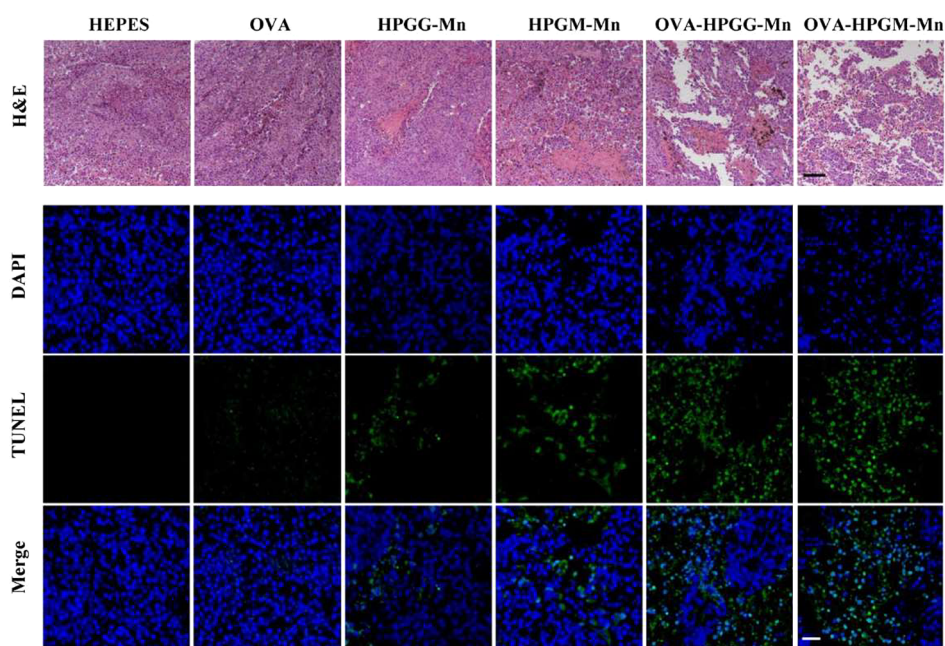
Figure 6. H&E staining images (scale bar = 100 μm) and TUNEL staining images (scale bar = 50 μm) of tumors with different treatments.

adjuvant with OVA antigen deserve further in-depth investigation to get deeper understanding in our ongoing work.[58−60]

In Vivo Nanovaccine Retention and Antitumor Immune Activity. The nanovaccine retention ability in vivo and drainage into lymph nodes is key to play immune-priming activity. Fluorescence intensity changes of free FITC-labeled OVA, OVA-HPGG-Mn, and OVA-HPGM-Mn in mice were recorded by on-line fluorescence imaging for 72 h (Figure S7). The fluorescence of free FITC-labeled OVA decayed quickly and grew weaker than that of the nanovaccine groups at 6 h and completely disappeared at 72 h, indicating that free FITC-OVA was cleared rapidly over the blood circulation. However, both OVA-HPGG-Mn and OVA-HPGM-Mn nanovaccines retained strong fluorescence at the injection site even for 72 h, suggesting that the glycopolypeptide coordinated nanovaccines effectively extended the residence time of antigen in vivo, which would prolong immune stimulation and help to enhance the immune response.[61,62] As a note, the mannose-tethered nanovaccine produced a relatively stronger fluorescence than the glucose-modified one in vivo, which was consistent with the above results in vitro. In addition, negligible fluorescence could be observed in the lymph nodes of mice by using on-line fluorescent microscopy. This suggests that the glycopolypeptide nanovaccines >200 nm injected at the mice tail were difficult to drain into the lymph nodes of mice, which was consistent with previous work.[63,64] And the optimization design and size modulation of the glycopolypeptide coordinated nanovaccines need to be further studied in our ongoing project.

We then evaluated the antitumor immune activity of the above nanovaccines using the B16-OVA melanoma tumor model. As shown in Figure 5a, the B16-OVA tumor-bearing mice were divided into six groups and respectively treated with HEPES, OVA, HPGG-Mn, HPGM-Mn, OVA-HPGG-Mn, and OVA-HPGM-Mn on days 6, 10, and 14 near the tumors by subcutaneous injection. The tumor size and body weight of each mouse were monitored during the whole therapeutic

period. On day 19, tumors were removed from mice and weighted; the results were displayed in Figure 5b−d. Obviously, free OVA could not inhibit tumor growth at a dose of 50 μg/per mouse, showing negligible immune activity in vivo, while tumor growth was slightly delayed in HPGG-Mn and PHGM-Mn groups due to the effect of self-adjuvant. Moreover, the comparison of tumor weight showed that the tumors in the HPGM-Mn group were lighter than those in HEPES, OVA, and HPGG-Mn, probably because the mannose-tethered HPGM-Mn could specifically target DCs, thus relatively inhibiting tumor growth. The tumor growth in the OVA-HPGG-Mn and OVA-HPGM-Mn groups was obviously delayed, and OVA-HPGM-Mn exhibited the strongest antitumor efficacy with tumor inhibition rate of ~80%, indicating that the mannose-tethered nanovaccine primed relatively potent anti-tumor immunity. There was no obvious change of mice weight during the whole experiments, demonstrating negligible toxicity of those nanovaccines (Figure 5e). The heart, liver, spleen, lungs, and kidneys were separated, and H&E staining was shown in Figure S8; no obvious pathological changes were observed, indicating the biosafety of the glycopolypeptide nanovaccines in vivo. In addition, in vivo immune prevention and rechallenge experiments deserve to be studied for the optimization of these glycopolypeptide nanovaccines such as the immunization doses and intervals to achieve high immune potency.

To further evaluate the antitumor efficacy of nanovaccines in vivo, the cell apoptosis in the dissected tumors post-treatment was measured by H&E and TUNEL staining techniques. As shown in Figure 6, the cell apoptosis in the HPGG-Mn and HPGM-Mn groups was clearly observed in H&E and TUNEL images, demonstrating that the blank glycopolypeptide coordinated nanoparticles in vivo indeed played self-adjuvant activities to induce tumor apoptosis, which was basically consistent with in vitro study. Much heavier cell apoptosis in OVA-HPGG-Mn and OVA-HPGM-Mn was observed, indicating the loaded OVA antigen could implement more potent antitumor effect with the assistance of the glycopolypeptide
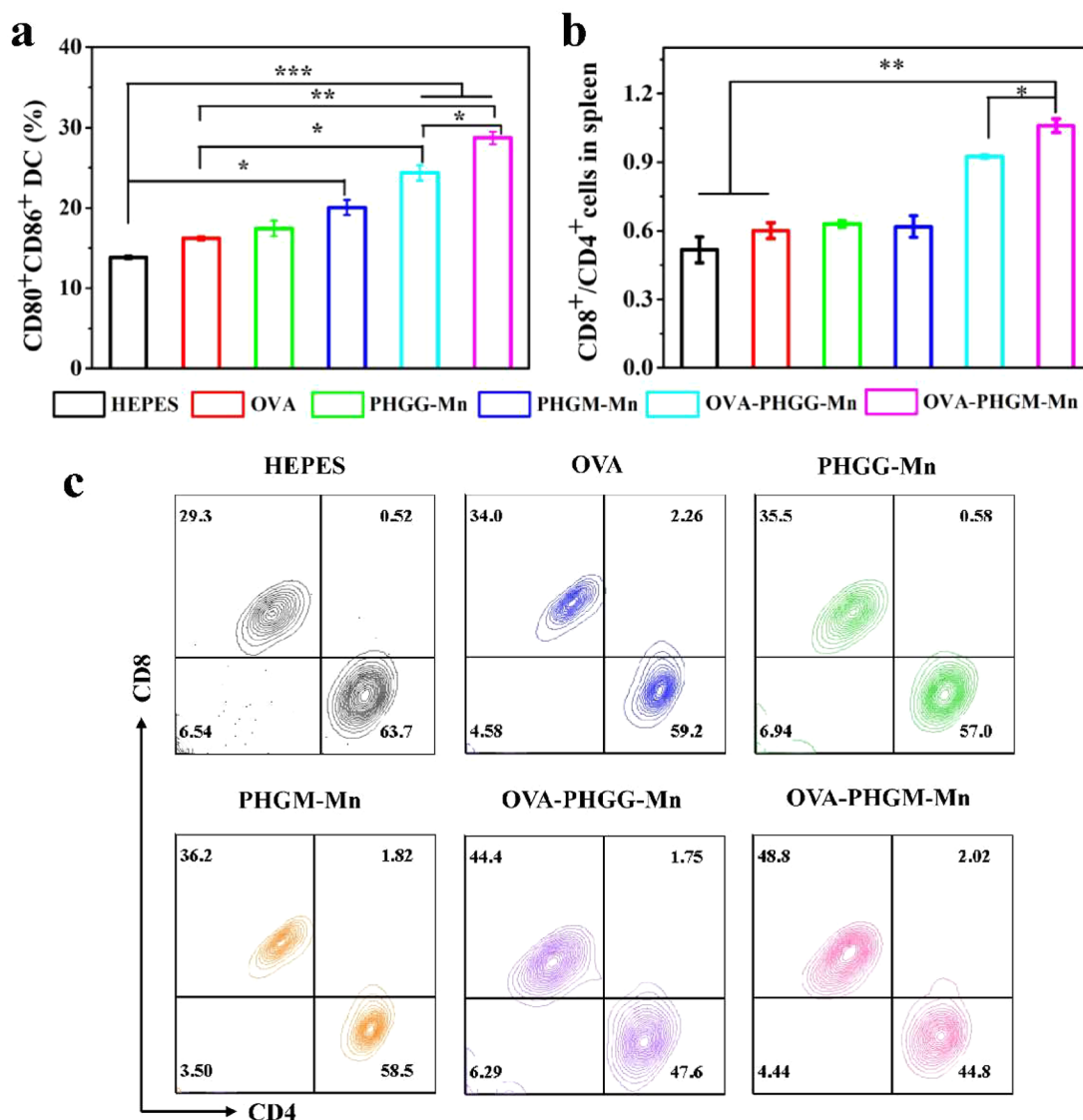
Figure 7. (a) Quantification of $CD80^+CD86^+$ DCs in inguinal lymph nodes and (b) the ratio of $CD8^+/CD4^+$T cells in the spleen ($n = 3$, $p^* < 0.05$, $p^{**} < 0.01$, $P^{***} < 0.001$). (c) Flow cytometric analyses of the populations of $CD8^+$T and $CD4^+$T cells in the splenocytes of C57BL/6 mice after various treatments.

nanocarrier as self-adjuvant. A similar phenomenon was observed in previous reports while comparative adjuvant potency with microstructure/size relationship needs further investigation.[65,66]

To analyze whether an antitumor effect in vivo was induced by adaptive immune responses, the immunological evaluation on the lymph nodes (LNs), spleens, tumors, and serum was performed after treatment. The proportions of $CD80^+CD86^+$ mature DCs in inguinal lymph nodes were detected by flow cytometry. As shown in Figure S9 and Figure 7a, HPGG-Mn and HPGM-Mn increased the proportion of mature DCs to 19.4% and 21.0%, respectively; OVA-HPGG-Mn and OVA-HPGM-Mn further promoted the maturation level of DCs up to 23.4% and 29.5%, respectively, indicating the immune priming activities of these nanovaccines in vivo. The ratio of $CD4^+$ and $CD8^+$ T cells in the spleen after different treatments was analyzed by flow cytometry, and the results were shown in Figure 7b,c. The percentage of $CD8^+$ T in the HPGG-Mn and HPGM-Mn groups was 35.5% and 36.2%, respectively, slightly more than 29.3% in the HEPES control; however, the ratio of

OVA-HPGG-Mn and OVA-HPGM-Mn groups reached to 44.4% and 48.8%, boosting the $CD8^+/CD4^+$ ratio increase to 0.92 for OVA-HPGG-Mn and 1.06 for OVA-HPGM-Mn from 0.52 for HEPES. These results evidence that the glycopolypeptide coordinated nanovaccines could prime the maturation of antigen-presenting DC cells and further activate $CD8^+/CD4^+$T cells immunity. It is noteworthy that comprehensive analyses on infiltrated $CD4^+/CD8^+$T, regulatory T cells (Tregs), and tumor-asscociated macrophages (TAM) in tumors need in-depth investigation for our glycopolypeptide coordinated nanovaccine to understand the immune stimulation and the immune regulation on the tumor microenvironment.

Furthermore, immunofluorescence images in Figure 8a also showed that $CD8^+$T cell response was dramatically enhanced when treated with OVA-HPGG-Mn or OVA-HPGM-Mn, indicating those nanovaccines remarkably induced adaptive immune response of T cells.[67,68] Note that the blank nanocarriers of HPGG-Mn and HPGM-Mn also played their adjuvant roles, which was consistent with the above in vivo tumor inhibition, H&E, and TUNEL analyses. The biomarkers
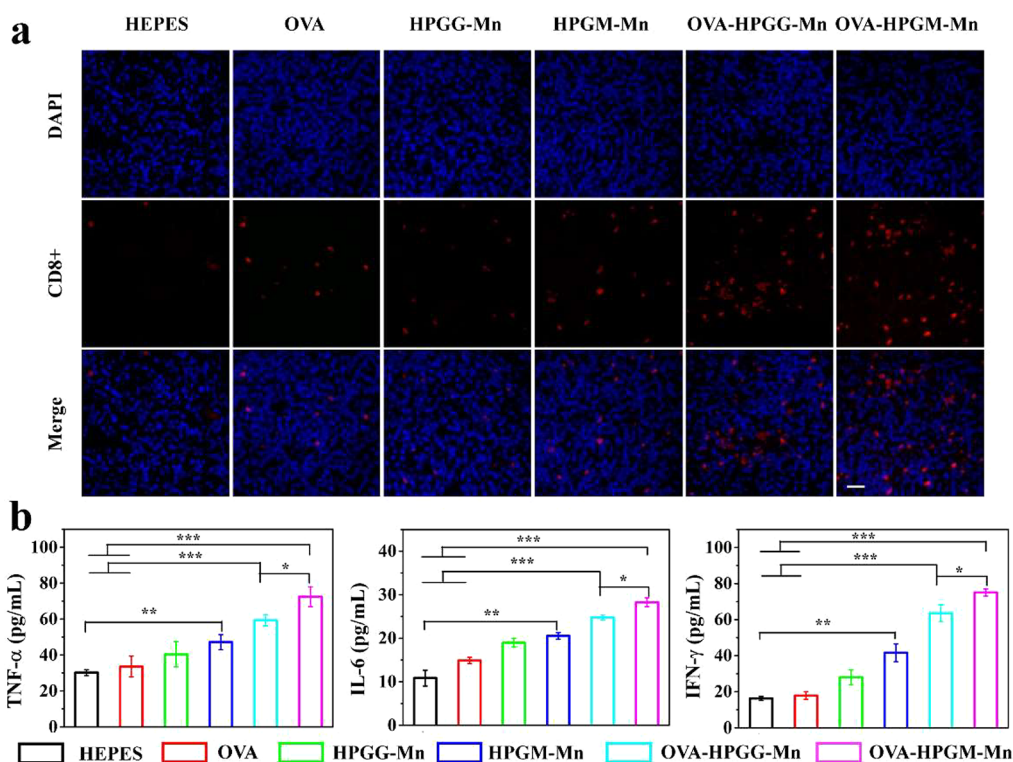
Figure 8. (a) Immunofluorescence staining images of CD8 (red) in tumors after various treatments (scale bar = 100 μm); (b) the cytokines concentrations of TNF-α, IL-6, and IFN-γ in the mice serum after various treatments ($n = 3$, $p^* < 0.05$, $p^{**} < 0.01$, $P^{***} < 0.001$).

for adaptive cellular immunity including IFN-γ, IL-6, and TNF-α in serum were determined by ELISA.[69,70] As shown in Figure 8b, IFN-γ, IL-6, and TNF-α were slightly upregulated after treated with HPGG-Mn or HPGM-Mn compared to HEPES and free OVA but significantly increased in OVA-HPGG-Mn and OVA-HPGM-Mn; the levels of IFN-γ, IL-6, and TNF-α in OVA-HPGM-Mn were higher than those in OVA-HPGG-Mn ($P < 0.05$), further evidencing the mannose-tethered nanovaccine induced more potent immune activity. Collectively, all these results demonstrate that the mannose-tethered glycopolypeptide coordinated nanovaccine could prime the maturation of DCs in lymph nodes, activate CD4$^+$/CD8$^+$T cells in spleen, and upregulate pro-inflammatory cytokines in serum, thus achieving a relatively potent immune response to delay the tumor growth in vivo.

CONCLUSION

In summary, we synthesized a kind of glycopolypeptide bearing histidine side chain with multiple sugar binding moieties and facilely constructed their OVA-loaded Mn^{2+}-coordinated nanovaccines with ~30% of the OVA-loading capacity. The mannose-tethered nanovaccine of OVA-HPGM-Mn could specifically deliver OVA to DCs and effectively promote OVA trafficking from endolysosomes to cytoplasm, thus inducing DCs maturation with the assistance of blank nanocarrier as a self-adjuvant. Moreover, the OVA-HPGM-Mn nanovaccine prolonged the retention time of the OVA for 72 h in mice, activated DCs maturation in lymph nodes, primed adaptive CD4$^+$/CD8$^+$T cells immunity in the spleen, upregulated pro-inflammatory cytokines in serum, and inhibited ~80% tumor growth in vivo. Hopefully, this work provides a useful platform for constructing the glycopolypeptide coordinated nanovaccines for cancer immunotherapy.

ASSOCIATED CONTENT

Ⓢ Supporting Information

The Supporting Information is available free of charge at https://pubs.acs.org/doi/10.1021/cbe.4c00083.

NCA monomer synthesis, Scheme S1, Figures S1−S9 (PDF)

AUTHOR INFORMATION

Corresponding Author

Chang-Ming Dong − *School of Chemistry and Chemical Engineering, Frontiers Science Center for Transformative Molecules, Shanghai Key Laboratory of Electrical Insulation and Thermal Aging, Shanghai Jiao Tong University, Shanghai 200240, P. R. China;* ⓞ orcid.org/0000-0002-7540-1082; Email: cmdong@sjtu.edu.cn

Authors

Yingying Song − *School of Chemistry and Chemical Engineering, Frontiers Science Center for Transformative Molecules, Shanghai Key Laboratory of Electrical Insulation and Thermal Aging, Shanghai Jiao Tong University, Shanghai 200240, P. R. China*

Lin Teng − *School of Chemistry and Chemical Engineering, Frontiers Science Center for Transformative Molecules, Shanghai Key Laboratory of Electrical Insulation and Thermal Aging, Shanghai Jiao Tong University, Shanghai 200240, P. R. China*

Yanzheng Chen − *School of Chemistry and Chemical Engineering, Frontiers Science Center for Transformative Molecules, Shanghai Key Laboratory of Electrical Insulation and Thermal Aging, Shanghai Jiao Tong University, Shanghai 200240, P. R. China*

Complete contact information is available at:
https://pubs.acs.org/10.1021/cbe.4c00083

Notes

The authors declare no competing financial interest.

■ REFERENCES

(1) Taefehshokr, S.; Parhizkar, A.; Hayati, S.; Mousapour, M.; Mahmoudpour, A.; Eleid, L.; Rahmanpour, D.; Fattahi, S.; Shabani, H.; Taefehshokr, N. Cancer Immunotherapy: Challenges and Limitations. *Pathology - Research and Practice* **2022**, *229*, 153723.

(2) Tan, S.; Li, D.; Zhu, X. Cancer Immunotherapy: Pros, Cons and Beyond. *Biomedicine & Pharmacotherapy* **2020**, *124*, 109821.

(3) Banstola, A.; Jeong, J.-H.; Yook, S. Immunoadjuvants for Cancer Immunotherapy: A Review of Recent Developments. *Acta Biomaterialia* **2020**, *114*, 16−30.

(4) Shiravand, Y.; Khodadadi, F.; Kashani, S. M. A.; Hosseini-Fard, S. R.; Hosseini, S.; Sadeghirad, H.; Ladwa, R.; O'Byrne, K.; Kulasinghe, A. Immune Checkpoint Inhibitors in Cancer Therapy. *Current Oncology* **2022**, *29* (5), 3044−3060.

(5) Lin, M. J.; Svensson-Arvelund, J.; Lubitz, G. S.; Marabelle, A.; Melero, I.; Brown, B. D.; Brody, J. D. Cancer Vaccines: The next Immunotherapy Frontier. *Nat. Cancer* **2022**, *3* (8), 911−926.

(6) Yu, J. X.; Upadhaya, S.; Tatake, R.; Barkalow, F.; Hubbard-Lucey, V. M. Cancer Cell Therapies: The Clinical Trial Landscape. *Nat. Rev. Drug Discov* **2020**, *19* (9), 583−584.

(7) Jin, S.; Sun, Y.; Liang, X.; Gu, X.; Ning, J.; Xu, Y.; Chen, S.; Pan, L. Emerging New Therapeutic Antibody Derivatives for Cancer Treatment. *Sig Transduct Target Ther* **2022**, *7* (1), 39.

(8) Wang, C.; Ye, Y.; Hu, Q.; Bellotti, A.; Gu, Z. Tailoring Biomaterials for Cancer Immunotherapy: Emerging Trends and Future Outlook. *Advanced Materials* **2017**, *29* (29), 1606036.

(9) Fang, R. H.; Hu, C.-M. J.; Luk, B. T.; Gao, W.; Copp, J. A.; Tai, Y.; O'Connor, D. E.; Zhang, L. Cancer Cell Membrane-Coated Nanoparticles for Anticancer Vaccination and Drug Delivery. *Nano Lett.* **2014**, *14* (4), 2181−2188.

(10) Zhao, Y.; Baldin, A. V.; Isayev, O.; Werner, J.; Zamyatnin, A. A.; Bazhin, A. V. Cancer Vaccines: Antigen Selection Strategy. *Vaccines* **2021**, *9* (2), 85.

(11) Filipić, B.; Pantelić, I.; Nikolić, I.; Majhen, D.; Stojić-Vukanić, Z.; Savić, S.; Krajišnik, D. Nanoparticle-Based Adjuvants and Delivery Systems for Modern Vaccines. *Vaccines* **2023**, *11* (7), 1172.

(12) Bezbaruah, R.; Chavda, V. P.; Nongrang, L.; Alom, S.; Deka, K.; Kalita, T.; Ali, F.; Bhattacharjee, B.; Vora, L. Nanoparticle-Based Delivery Systems for Vaccines. *Vaccines* **2022**, *10* (11), 1946.

(13) Cai, J.; Wang, H.; Wang, D.; Li, Y. Improving Cancer Vaccine Efficiency by Nanomedicine. *Adv. Biosys.* **2019**, *3* (3), 1800287.

(14) Li, X.; Yang, W.; Zou, Y.; Meng, F.; Deng, C.; Zhong, Z. Efficacious Delivery of Protein Drugs to Prostate Cancer Cells by PSMA-Targeted pH-Responsive Chimaeric Polymersomes. *Journal of Controlled Release* **2015**, *220*, 704−714.

(15) Liu, G.; Ma, S.; Li, S.; Cheng, R.; Meng, F.; Liu, H.; Zhong, Z. The Highly Efficient Delivery of Exogenous Proteins into Cells Mediated by Biodegradable Chimaeric Polymersomes. *Biomaterials* **2010**, *31* (29), 7575−7585.

(16) Shae, D.; Baljon, J. J.; Wehbe, M.; Christov, P. P.; Becker, K. W.; Kumar, A.; Suryadevara, N.; Carson, C. S.; Palmer, C. R.; Knight, F. C.; Joyce, S.; Wilson, J. T. Co-Delivery of Peptide Neoantigens and Stimulator of Interferon Genes Agonists Enhances Response to Cancer Vaccines. *ACS Nano* **2020**, *14* (8), 9904−9916.

(17) Li, P.; Shi, G.; Zhang, X.; Song, H.; Zhang, C.; Wang, W.; Li, C.; Song, B.; Wang, C.; Kong, D. Guanidinylated Cationic Nanoparticles as Robust Protein Antigen Delivery Systems and Adjuvants for Promoting Antigen-Specific Immune Responses in Vivo. *J. Mater. Chem. B* **2016**, *4* (33), 5608−5620.

(18) Wang, C.; Sun, P.; Wang, G.; Yuan, P.; Jiang, R.; Wang, W.; Huang, W.; Fan, Q. Conjugated Polymer Brush Based on Poly(l-Lysine) with Efficient Ovalbumin Delivery for Dendritic Cell Vaccine. *ACS Appl. Bio Mater.* **2018**, *1* (6), 1972−1982.

(19) Chang, H.; Lv, J.; Gao, X.; Wang, X.; Wang, H.; Chen, H.; He, X.; Li, L.; Cheng, Y. Rational Design of a Polymer with Robust Efficacy for Intracellular Protein and Peptide Delivery. *Nano Lett.* **2017**, *17* (3), 1678−1684.

(20) Sharpe, L. A.; Vela Ramirez, J. E.; Haddadin, O. M.; Ross, K. A.; Narasimhan, B.; Peppas, N. A. pH-Responsive Microencapsulation Systems for the Oral Delivery of Polyanhydride Nanoparticles. *Biomacromolecules* **2018**, *19* (3), 793−802.

(21) Morimoto, N.; Hirano, S.; Takahashi, H.; Loethen, S.; Thompson, D. H.; Akiyoshi, K. Self-Assembled pH-Sensitive Cholesteryl Pullulan Nanogel As a Protein Delivery Vehicle. *Biomacromolecules* **2013**, *14* (1), 56−63.

(22) Zhao, H.; Xu, J.; Li, Y.; Guan, X.; Han, X.; Xu, Y.; Zhou, H.; Peng, R.; Wang, J.; Liu, Z. Nanoscale Coordination Polymer Based Nanovaccine for Tumor Immunotherapy. *ACS Nano* **2019**, *13* (11), 13127−13135.

(23) Hao, P.; Wu, X.; Wang, L.; Wei, S.; Xu, H.; Huang, W.; Li, Y.; Zhang, T.; Zan, X. One-Pot Generating Subunit Vaccine with High Encapsulating Efficiency and Fast Lysosome Escape for Potent Cellular Immune Response. *Bioconjugate Chem.* **2020**, *31* (8), 1917−1927.

(24) Liu, K.; Tao, Y.; Wang, L.; Lei, J.; Liu, J.; Liu, Q. A Novel Multifunctional Vaccine Platform with Dendritic Cell-Targeting and pH-Responsive for Cancer Immunotherapy: Antigen-Directed Biomimetic Fabrication of a Cabbage-like Mannatide-Zinc-Antigen Hybrid Microparticles. *Chemical Engineering Journal* **2021**, *426*, 130867.

(25) Andreini, C.; Bertini, I.; Cavallaro, G.; Holliday, G. L.; Thornton, J. M. Metal Ions in Biological Catalysis: From Enzyme Databases to General Principles. *J. Biol. Inorg. Chem.* **2008**, *13* (8), 1205−1218.

(26) Liu, J.; Chakraborty, S.; Hosseinzadeh, P.; Yu, Y.; Tian, S.; Petrik, I.; Bhagi, A.; Lu, Y. Metalloproteins Containing Cytochrome, Iron−Sulfur, or Copper Redox Centers. *Chem. Rev.* **2014**, *114* (8), 4366−4469.

(27) Song, Y.; Liu, Y.; Teo, H. Y.; Hanafi, Z. B.; Mei, Y.; Zhu, Y.; Chua, Y. L.; Lv, M.; Jiang, Z.; Liu, H. Manganese Enhances the Antitumor Function of CD8+ T Cells by Inducing Type I Interferon Production. *Cell Mol. Immunol* **2021**, *18* (6), 1571−1574.

(28) Lv, M.; Chen, M.; Zhang, R.; Zhang, W.; Wang, C.; Zhang, Y.; Wei, X.; Guan, Y.; Liu, J.; Feng, K.; Jing, M.; Wang, X.; Liu, Y.-C.; Mei, Q.; Han, W.; Jiang, Z. Manganese Is Critical for Antitumor Immune Responses via cGAS-STING and Improves the Efficacy of Clinical Immunotherapy. *Cell Res.* **2020**, *30* (11), 966−979.

(29) Xu, C.; Dobson, H. E.; Yu, M.; Gong, W.; Sun, X.; Park, K. S.; Kennedy, A.; Zhou, X.; Xu, J.; Xu, Y.; Tai, A. W.; Lei, Y. L.; Moon, J. J. STING Agonist-Loaded Mesoporous Manganese-Silica Nanoparticles for Vaccine Applications. *Journal of Controlled Release* **2023**, *357*, 84−93.

(30) Sun, X.; Zhang, Y.; Li, J.; Park, K. S.; Han, K.; Zhou, X.; Xu, Y.; Nam, J.; Xu, J.; Shi, X.; Wei, L.; Lei, Y. L.; Moon, J. J. Amplifying STING Activation by Cyclic Dinucleotide−Manganese Particles for Local and Systemic Cancer Metalloimmunotherapy. *Nat. Nanotechnol.* **2021**, *16* (11), 1260−1270.

(31) OuYang, X.; Xu, X.; Qin, Q.; Dai, C.; Wang, H.; Liu, S.; Hu, L.; Xiong, X.; Liu, H.; Zhou, D. Manganese-Based Nanoparticle Vaccine for Combating Fatal Bacterial Pneumonia. *Advanced Materials* **2023**, *35* (51), 2304514.

(32) Wang, X.; Song, Z.; Wei, S.; Ji, G.; Zheng, X.; Fu, Z.; Cheng, J. Polypeptide-Based Drug Delivery Systems for Programmed Release. *Biomaterials* **2021**, *275*, 120913.

(33) Song, Y.; Ding, Y.; Dong, C.-M. Stimuli-Responsive Polypeptide Nanoassemblies: Recent Progress and Applications in

Cancer Nanomedicine. *WIREs Nanomed Nanobiotechnol* **2022**, *14* (2), e1742.

(34) Song, Y.; Chen, Y.; Li, P.; Dong, C.-M. Photoresponsive Polypeptide-Glycosylated Dendron Amphiphiles: UV-Triggered Polymersomes, OVA Release, and In Vitro Enhanced Uptake and Immune Response. *Biomacromolecules* **2020**, *21* (12), 5345−5357.

(35) Su, Y.; Xu, W.; Wei, Q.; Ma, Y.; Ding, J.; Chen, X. Chiral Polypeptide Nanoparticles as Nanoadjuvants of Nanovaccines for Efficient Cancer Prevention and Therapy. *Science Bulletin* **2023**, *68* (3), 284−294.

(36) Midoux, P.; Pichon, C.; Yaouanc, J.-J.; Jaffrès, P.-A. Chemical Vectors for Gene Delivery: A Current Review on Polymers, Peptides and Lipids Containing Histidine or Imidazole as Nucleic Acids Carriers. *British Journal of Pharmacology* **2009**, *157* (2), 166−178.

(37) Pyreddy, S.; Poddar, A.; Carraro, F.; Polash, S. A.; Dekiwadia, C.; Murdoch, B.; Nasa, Z.; Reddy, T. S.; Falcaro, P.; Shukla, R. Targeting Telomerase Utilizing Zeolitic Imidazole Frameworks as Non-Viral Gene Delivery Agents across Different Cancer Cell Types. *Biomaterials Advances* **2023**, *149*, 213420.

(38) Sun, B.; Zhao, X.; Wu, Y.; Cao, P.; Movahedi, F.; Liu, J.; Wang, J.; Xu, Z. P.; Gu, W. Mannose-Functionalized Biodegradable Nanoparticles Efficiently Deliver DNA Vaccine and Promote Anti-Tumor Immunity. *ACS Appl. Mater. Interfaces* **2021**, *13* (12), 14015−14027.

(39) Chen, J.; Fang, H.; Hu, Y.; Wu, J.; Zhang, S.; Feng, Y.; Lin, L.; Tian, H.; Chen, X. Combining Mannose Receptor Mediated Nanovaccines and Gene Regulated PD-L1 Blockade for Boosting Cancer Immunotherapy. *Bioactive Materials* **2022**, *7*, 167−180.

(40) Sun, L.; Ma, X.; Dong, C.-M.; Zhu, B.; Zhu, X. NIR-Responsive and Lectin-Binding Doxorubicin-Loaded Nanomedicine from Janus-Type Dendritic PAMAM Amphiphiles. *Biomacromolecules* **2012**, *13* (11), 3581−3591.

(41) Liu, D.-L.; Chang, X.; Dong, C.-M. Reduction- and Thermo-Sensitive Star Polypeptide Micelles and Hydrogels for on-Demand Drug Delivery. *Chem. Commun.* **2013**, *49* (12), 1229.

(42) Sun, L.; Zhu, B.; Su, Y.; Dong, C. M. Light-responsive linear-dendritic amphiphiles and their nanomedicines for NIR-triggered drug release. *Polym. Chem.* **2014**, *5*, 1605−1613.

(43) Lutz, M. B.; Kukutsch, N.; Ogilvie, A. L. J.; Rößner, S.; Koch, F.; Romani, N.; Schuler, G. An Advanced Culture Method for Generating Large Quantities of Highly Pure Dendritic Cells from Mouse Bone Marrow. *Journal of Immunological Methods* **1999**, *223* (1), 77−92.

(44) Madaan, A.; Verma, R.; Singh, A. T.; Jain, S. K.; Jaggi, M. A Stepwise Procedure for Isolation of Murine Bone Marrow and Generation of Dendritic Cells. *Journal of Biological Methods* **2014**, *1* (1), e1−e1.

(45) Sasidharan, A.; Panchakarla, L. S.; Sadanandan, A. R.; Ashokan, A.; Chandran, P.; Girish, C. M.; Menon, D.; Nair, S. V.; Rao, C. N. R.; Koyakutty, M. Hemocompatibility and Macrophage Response of Pristine and Functionalized Graphene. *Small* **2012**, *8* (8), 1251−1263.

(46) Semsarilar, M.; Ladmiral, V.; Perrier, S. Highly Branched and Hyperbranched Glycopolymers via Reversible Addition−Fragmentation Chain Transfer Polymerization and Click Chemistry. *Macromolecules* **2010**, *43* (3), 1438−1443.

(47) Huang, W.; Hao, P.; Qin, J.; Luo, S.; Zhang, T.; Peng, B.; Chen, H.; Zan, X. Hexahistidine-Metal Assemblies: A Promising Drug Delivery System. *Acta Biomaterialia* **2019**, *90*, 441−452.

(48) Chen, T.-T.; Yi, J.-T.; Zhao, Y.-Y.; Chu, X. Biomineralized Metal−Organic Framework Nanoparticles Enable Intracellular Delivery and Endo-Lysosomal Release of Native Active Proteins. *J. Am. Chem. Soc.* **2018**, *140* (31), 9912−9920.

(49) Li, Z.; Song, L. F.; Sharma, G.; Koca Fındık, B.; Merz, K. M., Jr. Accurate Metal−Imidazole Interactions. *J. Chem. Theory Comput.* **2023**, *19* (2), 619−625.

(50) Sun, W.; Tang, X.; Yang, Q.; Xu, Y.; Wu, F.; Guo, S.; Zhang, Y.; Wu, M.; Wang, Y. Coordination-Induced Interlinked Covalent- and

Metal−Organic-Framework Hybrids for Enhanced Lithium Storage. *Advanced Materials* **2019**, *31* (37), 1903176.

(51) Matanovic, I.; Babanova, S.; Perry, A., Iii; Serov, A.; Artyushkova, K.; Atanassov, P. Bio-Inspired Design of Electrocatalysts for Oxalate Oxidation: A Combined Experimental and Computational Study of Mn−N−C Catalysts. *Phys. Chem. Chem. Phys.* **2015**, *17* (20), 13235−13244.

(52) Asayama, S.; Sudo, M.; Nagaoka, S.; Kawakami, H. Carboxymethyl Poly(L-histidine) as a New pH-Sensitive Polypeptide To Enhance Polyplex Gene Delivery. *Mol. Pharmaceutics* **2008**, *5* (5), 898−901.

(53) Ding, J.; Chen, J.; Li, D.; Xiao, C.; Zhang, J.; He, C.; Zhuang, X.; Chen, X. Biocompatible Reduction-Responsive Polypeptide Micelles as Nanocarriers for Enhanced Chemotherapy Efficacy in Vitro. *J. Mater. Chem. B* **2013**, *1* (1), 69−81.

(54) Shi, G.-N.; Zhang, C.-N.; Xu, R.; Niu, J.-F.; Song, H.-J.; Zhang, X.-Y.; Wang, W.-W.; Wang, Y.-M.; Li, C.; Wei, X.-Q.; Kong, D.-L. Enhanced Antitumor Immunity by Targeting Dendritic Cells with Tumor Cell Lysate-Loaded Chitosan Nanoparticles Vaccine. *Biomaterials* **2017**, *113*, 191−202.

(55) Nahar, U. J.; Toth, I.; Skwarczynski, M. Mannose in Vaccine Delivery. *Journal of Controlled Release* **2022**, *351*, 284−300.

(56) Shi, M.; Zhang, J.; Huang, Z.; Chen, Y.; Pan, S.; Hu, H.; Qiao, M.; Chen, D.; Zhao, X. Stimuli-Responsive Release and Efficient siRNA Delivery in Non-Small Cell Lung Cancer by a Poly(L -Histidine)-Based Multifunctional Nanoplatform. *J. Mater. Chem. B* **2020**, *8* (8), 1616−1628.

(57) Lu, D.; An, Y.; Feng, S.; Li, X.; Fan, A.; Wang, Z.; Zhao, Y. Imidazole-Bearing Polymeric Micelles for Enhanced Cellular Uptake, Rapid Endosomal Escape, and On-Demand Cargo Release. *AAPS PharmSciTech* **2018**, *19* (6), 2610−2619.

(58) Song, Y.; Dong, C. M. Sugar-dependent targeting and immune adjuvant effects of hyperbranched glycosylated polypeptide nano-particles for ovalbumin delivery. *Chinese Chemical Letters* **2022**, *33*, 4084−4088.

(59) Song, Y.; Ge, W.; Dong, C. M. Glycosylated Polypeptide Nanovesicles: Fabrication, Protein and Agonist Codelivery and Immune Activity. *Acta Polym. Sin.* **2023**, *54* (10), 1533−1546.

(60) HogenEsch, H.; O'Hagan, D. T.; Fox, C. B. Optimizing the utilization of aluminum adjuvants in vaccines: you might just get what you want. *npj Vaccines* **2018**, *3* (1), 51.

(61) Henriksen-Lacey, M.; Bramwell, V. W.; Christensen, D.; Agger, E.-M.; Andersen, P.; Perrie, Y. Liposomes Based on Dimethyldiocta-decylammonium Promote a Depot Effect and Enhance Immunogenicity of Soluble Antigen. *Journal of Controlled Release* **2010**, *142* (2), 180−186.

(62) Brewer, K. D.; Lake, K.; Pelot, N.; Stanford, M. M.; DeBay, D. R.; Penwell, A.; Weir, G. M.; Karkada, M.; Mansour, M.; Bowen, C. V. Clearance of Depot Vaccine SPIO-Labeled Antigen and Substrate Visualized Using MRI. *Vaccine* **2014**, *32* (51), 6956−6962.

(63) Chen, Y.; De Koker, S.; De Geest, B. G. Engineering Strategies for Lymph Node Targeted Immune Activation. *Accounts of chemical research* **2020**, *53* (10), 2055−2067.

(64) Manolova, V.; Flace, A.; Bauer, M.; Schwarz, K.; Saudan, P.; Bachmann, M. F. Nanoparticles Target Distinct Dendritic Cell Populations According to Their Size. *European journal of immunology* **2008**, *38* (5), 1404−1413.

(65) Zhang, X.; Wang, K.; Gao, Z.; Wu, Z.; Liu, W.; Li, J.; Gao, H.; Wei, J.; Ding, D.; Zheng, W. An Aggregation-Induced Emission Molecule-Assembled Nanovaccine with Self-Adjuvanted Function for Cancer Immunotherapy. *Adv. Funct. Mater.* **2023**, *33* (51), 2302118.

(66) Zhang, X.; Wang, K.; Zhao, Z.; Shan, X.; Wang, Y.; Feng, Z.; Li, B.; Luo, C.; Chen, X.; Sun, J. Self-Adjuvanting Polyguanidine Nanovaccines for Cancer Immunotherapy. *ACS Nano* **2024**, *18*, 7136−7147.

(67) Feng, B.; Zhou, F.; Hou, B.; Wang, D.; Wang, T.; Fu, Y.; Ma, Y.; Yu, H.; Li, Y. Binary Cooperative Prodrug Nanoparticles Improve Immunotherapy by Synergistically Modulating Immune Tumor Microenvironment. *Advanced Materials* **2018**, *30* (38), 1803001.

(68) Ding, B.; Zheng, P.; Jiang, F.; Zhao, Y.; Wang, M.; Chang, M.; Ma, P.; Lin, J. MnOx Nanospikes as Nanoadjuvants and Immunogenic Cell Death Drugs with Enhanced Antitumor Immunity and Antimetastatic Effect. *Angew. Chem., Int. Ed.* **2020**, *59* (38), 16381−16384.

(69) Zhang, Y.; Wang, F.; Ju, E.; Liu, Z.; Chen, Z.; Ren, J.; Qu, X. Metal-Organic-Framework-Based Vaccine Platforms for Enhanced Systemic Immune and Memory Response. *Adv. Funct. Mater.* **2016**, *26* (35), 6454−6461.

(70) Zhang, H.; Zhang, J.; Li, Q.; Song, A.; Tian, H.; Wang, J.; Li, Z.; Luan, Y. Site-Specific MOF-Based Immunotherapeutic Nanoplatforms via Synergistic Tumor Cells-Targeted Treatment and Dendritic Cells-Targeted Immunomodulation. *Biomaterials* **2020**, *245*, 119983.